Publication III

Ranran Lin, Ari Haavisto, and Antero Arkkio. 2010. Analysis of eddy-current loss in end shield and frame of a large induction machine. IEEE Transactions on Magnetics, volume 46, number 3, pages 942-948.

Analysis of Eddy-Current Loss in End Shield and Frame of a Large Induction Machine

Ranran Lin, Ari Haavisto, and Antero Arkkio

Department of Electrical Engineering, Faculty of Electronics, Communications and Automation, School of Science and Technology, Aalto University, Espoo, Finland

This paper proposes an effective method of analyzing the eddy-current loss within the end shield and frame of an electric machine. The standard impedance boundary condition is applied to the conducting surfaces of complete 3-D models, and the models are solved by time-harmonic finite-element analyses. Measurement of the temperature rise is completed as a validation of the proposed method. The effect of the distances between the conducting surfaces and coil ends is studied by computing the eddy-current loss for a series of 3-D models having different distances. In addition, simplified 2-D models are used to study the influence of material nonlinearity. In brief, the proposed method is feasible in computing the eddy-current loss. The eddy-current loss within the regions close to the coil ends is larger than the other regions in the end shield and frame, but the total loss is quite small, compared, for instance, with the copper loss within the stator winding. Furthermore, the farther the end shield and frame are from the coil ends, the smaller the eddy-current loss is. Finally, it is found that the eddy-current loss is larger in the nonlinear case than in the linear case.

***Index Terms*—Eddy current, end shield, finite-element analysis, frame, measurement, standard impedance boundary condition.**

I. Introduction

In a radial-flux rotating electric machine, the magnetic flux caused by the current flowing inside the stator end-winding is referred to as stator end-winding leakage. Albeit small in comparison with the main flux, it may lead to harmful phenomena, e.g., eddy current and mechanical vibration in the end region, magnetic force on the end-winding, etc. For modern large turbogenerators, to design them to minimize the effect of the stator end-winding leakage is one of the requirements [1]. In addition, for an induction motor working in a field-weakening region where there is a voltage constraint, the end-winding leakage reactance is an important parameter during the determination of the torque-speed characteristic.

The main structures where the eddy current flows include the frame and end shield as well as the clamping plates, clamping fingers, and retaining rings in large turbogenerators. The eddy current also occurs inside the laminations of the core ends. The above-mentioned eddy current gives rise to additional loss, which may affect the efficiency of the machine, and the generation of heat, which goes further to cause certain hot spots in the structures of the end region [2].

In the past two decades, some studies of the eddy current induced by the end-winding leakage were completed and most of them were focused on large turbogenerators [1]–[13].

References [1], [3]–[6] analyzed the eddy current induced inside the laminations of the stator core end by the stator end-winding. Moreover, [7]–[11] analyzed the eddy current in other structures of the end region, e.g., the clamping plates, clamping fingers, etc. On the other hand, the eddy current inside the rotor core end was also studied in [12] and [13]. Because of the complex structure of the end region, the finite-element method (FEM) was applied to all the above studies.

Manuscript received March 30, 2009; revised August 10, 2009. First published October 06, 2009; current version published February 18, 2010. Corresponding author: R. Lin (e-mail: ranran.lin@gmail.com).

Color versions of one or more of the figures in this paper are available online at http://ieeexplore.ieee.org.

Digital Object Identifier 10.1109/TMAG.2009.2031173

In fact, during the calculation of the eddy current by FEM, the mesh division of a model is important. Because most structures in the end region possess high conductivity, the eddy current is mainly concentrated within a thin layer close to the surfaces of the structures due to the skin effect. Therefore, dense mesh division within the thin layer is required in order to model the eddy current accurately. For example, the conductivity of the steel frame of a machine is around 5×10^6 S/m, and the relative permeability approximates 1000, so the skin depth is around 1 mm at 50 Hz. As a result, in finite-element analyses (FEAs), large numbers of elements need generating so there is difficulty in solving such a large equation system.

In general, two approaches can be applied to the calculation of the eddy current in the end region by FEM. Firstly, the size of the model is reduced by using suitable boundary conditions so that dense mesh division becomes possible. For instance, in [5], only one slot pitch of the core end was modeled, so under the circumstances nonlinear time-stepping analyses can be carried out. Secondly, when the skin depth is far less than the thickness of the conducting structure, the standard impedance boundary condition (SIBC) can be enforced on its surface to exclude it from the model. Correspondingly, the eddy current is modeled as surface current. Reference [4] enforced the SIBC on the conducting surface, namely the stator end plate. Nevertheless, the SIBC is usually used under time-harmonic analyses.

This paper aims at the study of the eddy current within the frame and end shield so that the analysis can be used for optimum design of electric machines. Such a study has not been carried out by other authors yet.

A proposed method based on the use of the SIBC was applied to the study of the eddy current within the end shield and frame of a 2.24-MW induction machine. 3-D time-harmonic FEAs were completed, and the eddy-current loss was computed and compared under different axial and radial distances between the conducting surfaces and coil ends. In addition, by altering the above two parameters, 2-D time-stepping FEAs based on simplified 2-D axisymmetric linear and nonlinear models were carried out to find the effect of the frame and end shield with a nonlinear magnetization curve on the eddy-current loss.

TABLE I
MAIN SPECIFICATIONS OF TEST MACHINE

Parameter	Value
Rated power (MW)	2.24
Rated current (A)	830
Rated frequency (Hz)	50
Full length of stator core (mm)	1000
Outer diameter of stator core (mm)	980
Inner diameter of stator core (mm)	670
Number of pole pairs	2
Number of stator slots	72
Number of parallel branches of stator winding	4
Number of turns in series within stator coil	3
Coil span of stator coil (stator slot pitches)	16

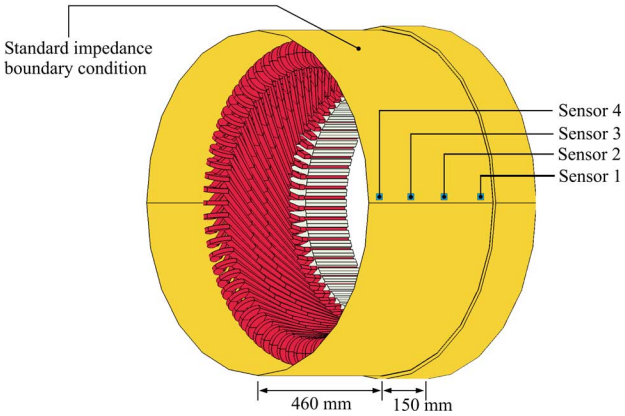

Fig. 1. The 3-D geometric model (without the air region) and the positions of the temperature sensors placed on the test machine.

II. 3-D ANALYSES OF EDDY CURRENT

A. 3-D Geometric Model and Numerical Model

A three-phase squirrel-cage induction machine with a form-wound two-layer diamond winding was studied. Table I lists its main specifications. Since it was impossible to test the machine at full load in the laboratory, the rotor parts were taken away and the stator parts were tested at the rated current.

The end shield and frame of the machine is made of steel whose skin depth is around 1 mm at the rated frequency. Though it was possible to do dense mesh division within a thin layer close to the inner surfaces of the end shield and frame, there was great difficulty in solving such a large equation system by a personal computer with a 2.66-GHz CPU and 8-GB RAM, due to the limit of the memory. Therefore, the SIBC was used to model the eddy current as surface current. Besides, to make good mesh division in the end region, only the 150-mm-long (axial direction) stator core end was included in the model according to the conclusion in [14] that only the end part of the active region is affected by the stator end-winding. Fig. 1 shows the 3-D geometric model.

B. Time-Harmonic FEAs

In the time-harmonic FEAs, the stator winding was supplied by three-phase current with the rms value $N\tilde{I}_{\rm ph}^{\rm str}/a$, where $\tilde{I}_{\rm ph}^{\rm str}$ is the rms value of the stator phase current; N is the number of turns in series within a stator coil; and a is the number of parallel branches of the stator winding. The governing equation was

$$\nabla\times[\boldsymbol{\nu}\cdot(\nabla\times\underline{\boldsymbol{A}})]+\mathrm{j}\omega\boldsymbol{\sigma}\cdot\underline{\boldsymbol{A}}-\underline{\boldsymbol{J}}_{\rm s}=0 \tag{1}$$

where $\underline{\boldsymbol{A}}$ and $\underline{\boldsymbol{J}}_{\rm s}$ are the complex vectors of magnetic vector potential and source current density, respectively; $\boldsymbol{\nu}$ and $\boldsymbol{\sigma}$ are the tensors of reluctivity and conductivity, respectively; and ω is an angular frequency. The end shield and frame were made of construction steel. In the 3-D time-harmonic analyses, its relative permeability was 1000. Electric scalar potential ϕ was not solved because the source current within the stator winding was known in the 3-D model which included the stator part only. Besides, the inclusion of ϕ would make the calculation carried out on the current computer not possible. As a separate study, a simpler model was built, and the eddy-current loss under the case with ϕ was a little smaller than without ϕ.

On the inner surface of the frame as shown in Fig. 1, the SIBC or the Leontovich boundary condition given by [15] was enforced:

$$\underline{\boldsymbol{E}}-(\boldsymbol{n}\cdot\underline{\boldsymbol{E}})\boldsymbol{n}=Z_{\rm s}\,\boldsymbol{n}\times\underline{\boldsymbol{H}} \tag{2}$$

where $\underline{\boldsymbol{E}}$ and $\underline{\boldsymbol{H}}$ are the complex vectors of electric field strength and magnetic field strength, respectively; $\boldsymbol{n}$ is an outward-directed normal unit vector on the surface; and $Z_{\rm s}$ is a surface impedance which is derived from

$$Z_{\rm s}=\sqrt{\frac{\mathrm{j}\omega\mu}{(\sigma+\mathrm{j}\omega\varepsilon)}}\approx\sqrt{\frac{\pi f\mu}{\sigma}}(1+\mathrm{j})\Bigg|_{\sigma\gg\omega\varepsilon} \tag{3}$$

where f denotes a frequency; μ,ε, and σ denote permeability, permittivity, and conductivity, respectively. The principle of the SIBC is based on the relations between the tangential components of an electric field and a magnetic field on the surface of a good conductor [16]. Detailed explanation for the SIBC can be found in [17].

Galerkin's method was used in the weak form of the method of weighted residual in order to construct the finite-element discretization.

C. Validation of 3-D Numerical Model

The validation of the 3-D model was carried out by two kinds of measurement in terms of the magnetic field and eddy-current loss, respectively.

1) Validation in Terms of Magnetic Field: A closed search coil made of enamelled copper wire was fixed along a coil end. The induced electromotive force (EMF) of the search coil was measured. The magnetic induction was also measured at two points. One point was in the end region, and the other in the active region.

In the 3-D model, a loop C, which was exactly the same as the search coil, was built. Under the time-harmonic analyses, the phasor of magnetic flux $\underline{\Phi}$ passing through the loop was derived from

$$\underline{\Phi}=\oint_{\rm C}\underline{\boldsymbol{A}}\cdot\mathrm{d}\boldsymbol{l} \tag{4}$$

TABLE II
RESULTS OF VALIDATION IN TERMS OF MAGNETIC FIELD

Region	Quantity	Calculation	Measurement
End region	$\tilde{\mathscr{E}}$ (V)	0.59	0.61
	$\tilde{B}_r$ (mT)	24.46	25.59
	$\tilde{B}_\varphi$ (mT)	26.77	28.68
	$\tilde{B}_z$ (mT)	26.33	28.63
Active region	$\tilde{B}_r$ (mT)	48.37	49.36
	$\tilde{B}_\varphi$ (mT)	47.90	45.35
	$\tilde{B}_z$ (mT)	3.63	6.53

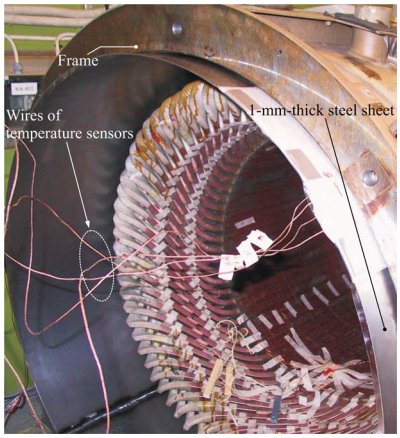

Fig. 2. The 1-mm-thick steel sheet inside the frame of the machine.

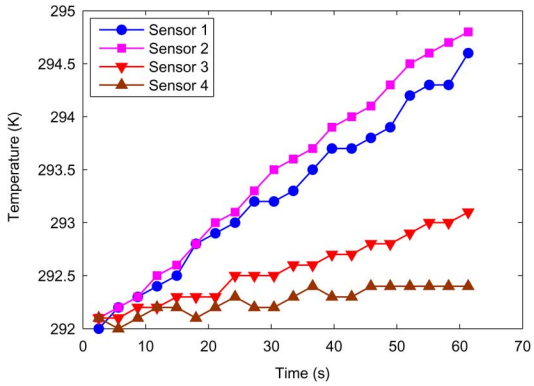

Fig. 3. The measurement results of the temperature in the steel sheet. The minimum change in temperature is 0.1 K.

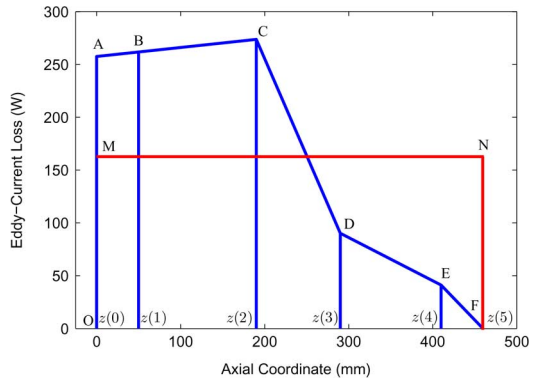

Fig. 4. The illustration of determining the measured average eddy-current loss.

where $\boldsymbol{l}$ is an arc length vector. According to Faraday's law, the phasor of an induced EMF $\underline{\mathscr{E}}$ was calculated as $\underline{\mathscr{E}} = -\mathrm{j}\omega\underline{\Phi}$, then its rms value was $|\underline{\mathscr{E}}|/\sqrt{2}$.

Table II lists the calculation and measurement results at the rated current. $\mathscr{E}$ means the rms value of the induced EMF, and $\tilde{B}_r, \tilde{B}_\varphi$, and $\tilde{B}_z$ mean the rms values of the radial, circumferential, and axial components of magnetic induction in the cylindrical coordinate system. In Table II, the calculations are consistent with the measurement results except $\tilde{B}_z$ at the point in the active region. The reason comes from the fact that it was difficult to make the probe of the meter exactly perpendicular to the direction of the measured component.

2) Validation in Terms of Eddy-Current Loss: Measuring the total loss within the machine was possible, but it was impossible to separate the loss within the end shield and frame from the total loss.

An approximate method of measuring the temperature rise was used to estimate the loss. At first, a 1-mm-thick, 460-mm-long (axial length) steel sheet was rolled up and put into the frame, as shown in Fig. 2. Afterwards heat insulation filler was put around it to reduce the heat transfer. In view of the small temperature difference between the winding and steel sheet, the thermal radiation was omitted. Therefore, the heat generated in the steel sheet was attributed to the eddy-current loss only.

Four temperature sensors were fixed to the steel sheet. The axial coordinate of one end of the steel sheet near the core was at $z(0) = 0$ mm. The four sensors were placed at $z(1) = 50$ mm, $z(2) = 190$ mm, $z(3) = 290$ mm, and $z(4) = 410$ mm, respectively, as marked in Fig. 1. The other end of the steel sheet was at $z(5) = 460$ mm. All the coordinates are marked in Fig. 4.

TABLE III
CALCULATIONS BASED ON MEASUREMENT OF TEMPERATURE

i	c_{steel} J/(kg·K)	m_{steel} (kg)	$\mathrm{d}T_i/\mathrm{d}t$ (K/s)	$\overline{P}_{\mathrm{Ft},i}$ (W)
1	500	11.05	0.047	261.8
2			0.050	273.7
3			0.016	90.2
4			0.007	41.2

The measurement lasted more than one minute, and Fig. 3 records the change in temperature. The four curves in Fig. 3 indicate that the distribution of the loss was not uniform in the steel sheet. The eddy-current loss corresponding to each curve was computed by

$$\bar{P}_{\mathrm{Ft},i} = c_{\mathrm{steel}} m_{\mathrm{steel}} \frac{\mathrm{d}T_i}{\mathrm{d}t}, \quad i = 1, 2, 3, 4, \tag{5}$$

where $\bar{P}_{\mathrm{Ft},i}$ is the average loss corresponding to the curve measured by sensor i; c_{steel} is the specific heat capacity of steel; m_{steel} is the mass of the steel sheet; T_i is the temperature measured by sensor i; and t is time. The value of $\mathrm{d}T_i/\mathrm{d}t$ corresponding to each curve was calculated by the regression analysis of the measured data obtained only during the first 25 s, because the influence of heat transfer on $\mathrm{d}T_i/\mathrm{d}t$ was not distinct in the first 25 s. Table III lists the corresponding calculations.

The total eddy-current loss within the steel sheet is determined according to Fig. 4. The horizontal axis represents the axial coordinates of the steel sheet. The values of

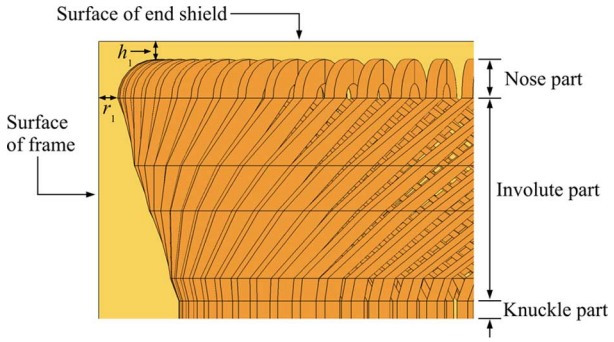

Fig. 5. Two locally defined variables r_1 and h_1 in the 3-D numerical models.

$\bar{P}_{\mathrm{Ft},1}, \bar{P}_{\mathrm{Ft},2}, \bar{P}_{\mathrm{Ft},3}$, and $\bar{P}_{\mathrm{Ft},4}$ listed in Table III are marked in Fig. 4 as points B, C, D, and E, respectively, where the sensors were placed. At one end of the steel sheet, $z(0)$, the loss is determined by extrapolating from line CB to point A and is calculated as $\bar{P}_{\mathrm{Ft},0} = 257.6$ W. At the other end, $z(5)$, the loss is assumed to be zero, i.e., $\bar{P}_{\mathrm{Ft},5} = 0$ W. The average total eddy-current loss $\bar{P}_{\mathrm{Ft,tot}}$ is calculated based on the fact that the area enclosed by line OMABCDEF and the horizontal axis is equal to the area enclosed by line OMNF and the horizontal axis in Fig. 4. $\bar{P}_{\mathrm{Ft,tot}}$ is actually the length of line OM and is calculated by

$$\bar{P}_{\mathrm{Ft,tot}} = \frac{1}{l_{\mathrm{steel}}} \sum_{n=0}^{4} \frac{1}{2} (\bar{P}_{\mathrm{Ft},n} + \bar{P}_{\mathrm{Ft},n+1})[z(n+1) - z(n)] \quad (6)$$

where l_{steel} is the axial length of the steel sheet.

On the other hand, in the FEAs, the 1-mm-thick steel sheet was modeled by the SIBC. This was an approximation because the skin depth of the steel sheet was 0.8 mm, which was not small by comparison with its thickness. However, since resistive loss is proportional to the square of current density, the loss calculated by the SIBC was considered as the eddy-current loss within the steel sheet, which was computed by

$$\bar{P}_{\mathrm{Ft,tot}} = \frac{1}{2} \int_{\Gamma_1} \mathrm{Re}\{\underline{\boldsymbol{J}}_{\mathrm{sur}} \cdot \underline{\boldsymbol{E}}^*\} \mathrm{d}S \quad (7)$$

where Γ_1 is the surfaces where the SIBC was enforced; Re means the real part of a complex number; $\underline{\boldsymbol{J}}_{\mathrm{sur}}$ and $\underline{\boldsymbol{E}}$ are the complex vectors of surface current density and electric field strength, respectively; $*$ denotes a complex conjugate; and S is a surface area.

According to (6), $\bar{P}_{\mathrm{Ft,tot}} \approx 165$ W, and from (7), $\bar{P}_{\mathrm{Ft,tot}} = 178.2$ W. The relative error is 8%, which is acceptable. The reasons for the error might result from some aspects, e.g., the accuracy of the mesh division, the accuracy of the temperature sensors, the installation of the sensors, etc.

In short, the 3-D model was validated from the aspects of both the magnetic field and eddy-current loss. As a result, the model with the SIBC and the linear magnetization curve was able to analyze the eddy current accurately.

D. Variation in Eddy-Current Loss

Two locally defined variables, the shortest axial distance h_1 between the nose part of a coil end and the surface of the end shield, and the shortest radial distance r_1 between the nose part and the surface of the frame, as marked in Fig. 5, were changed by shifting the surfaces, so a series of 3-D models were built. A minimum of 7 mm was chosen from the electrical insulation point of view. The eddy-current loss within the surfaces of the end shield and frame was calculated by (7) based on the same stator current.

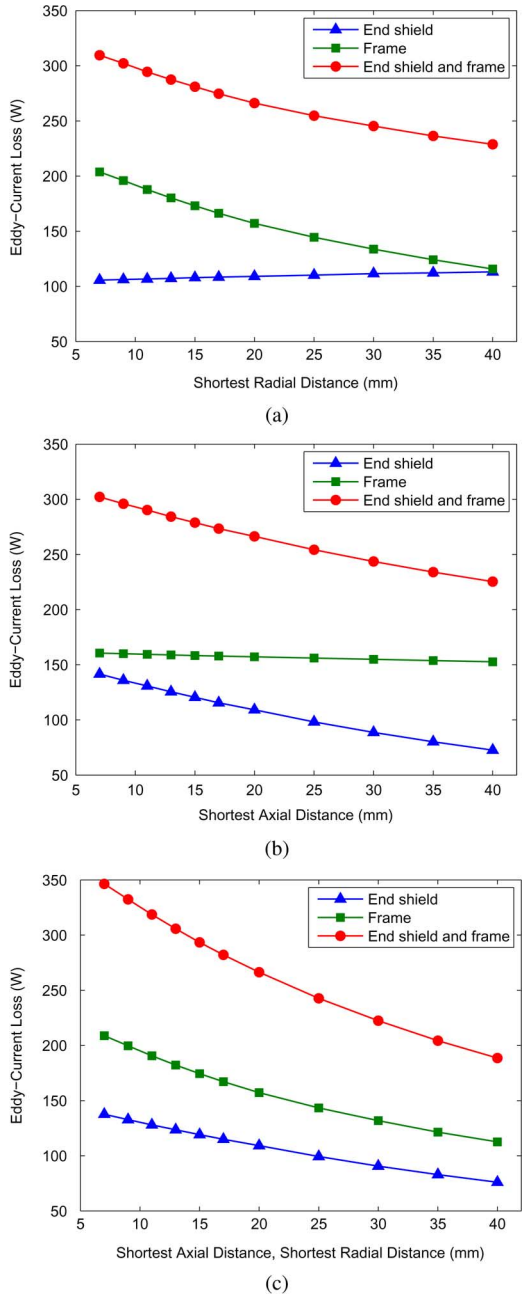

Fig. 6. The changes in the eddy-current loss within the surfaces of the end shield, frame, and both, of one end: (a) $7\,\mathrm{mm} \le r_1 \le 40\,\mathrm{mm}, h_1 \equiv 20\,\mathrm{mm}$; (b) $7\,\mathrm{mm} \le h_1 \le 40\,\mathrm{mm}, r_1 \equiv 20\,\mathrm{mm}$; (c) $7\,\mathrm{mm} \le r_1 \le 40\,\mathrm{mm}, 7\,\mathrm{mm} \le h_1 \le 40\,\mathrm{mm}, r_1 \equiv h_1$.

1) $7\,\mathrm{mm} \le r_1 \le 40\,\mathrm{mm}$, $h_1 \equiv 20\,\mathrm{mm}$: Fig. 6(a) plots the changes in the eddy-current loss within the surfaces of the end shield, frame, and both. The loss within the surface of the frame decreases obviously as r_1 increases, whereas there is a slight rise in the loss within the surface of the end shield. After adding up these two curves, the total loss shows an obvious decline as r_1 increases.

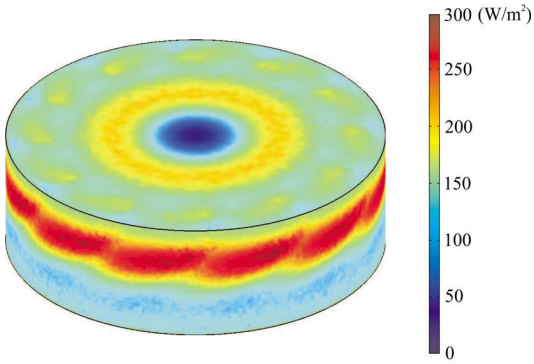

Fig. 7. The distribution of the time-average eddy-current loss density within the surfaces of the end shield and frame of one end. ($r_1 = h_1 = 20$ mm).

2) 7 mm $\leq h_1 \leq$ 40 mm, $r_1 \equiv$ 20 mm: The corresponding changes in the eddy-current loss are illustrated in Fig. 6(b). The three curves still represent the three cases mentioned above. When h_1 increases, a decrease in the loss within the surface of the end shield is evident whereas the loss within the surface of the frame is almost fixed.
3) 7 mm $\leq r_1 \leq$ 40 mm, 7 mm $\leq h_1 \leq$ 40 mm, $r_1 \equiv h_1$: The effect of the simultaneous changes of these two variables on the eddy-current loss is shown in Fig. 6(c). The loss inside all the parts declines as both r_1 and h_1 increase. No matter how r_1 and h_1 change, the eddy-current loss within the surface of the frame is larger than that within the surface of the end shield. Besides, the total eddy-current loss within both surfaces of one end is small, compared, for example, with the total copper loss within the stator winding 5.4 kW at the rated current. Even if r_1 and h_1 are equal to the minimum 7 mm, the total loss in one end is around 350 W, far smaller than 5.4 kW.

E. Distribution of Eddy Current and Its Loss Density

The distribution of the eddy-current loss within the end shield and frame was studied, since hot spots may appear in the regions where high loss density occurs. The distribution of the time-average eddy-current loss density within the surfaces of the end shield and frame of one end ($r_1 = h_1 = 20$ mm) is illustrated in Fig. 7. Relatively high loss density occurs within the surface of the frame that is near the connections between the nose parts and involute parts of the coil ends. Within the surface of the end shield around the center, there is almost no loss. Moreover, due to 12 phase belts of the stator winding, there are 12 clear repetitions in the distribution along the circumferential direction.

In addition, the distribution of the instantaneous eddy current within the surfaces of the end shield and frame ($r_1 = h_1 =$ 20 mm) is shown in Fig. 8. In Fig. 8(a), there are four main loops of the eddy current relating to the four poles in the model. In Fig. 8(b), there is one loop of the eddy current, since the surface of the frame in Fig. 8(b) just corresponds to one pole pitch. The distribution within the other surfaces is similar.

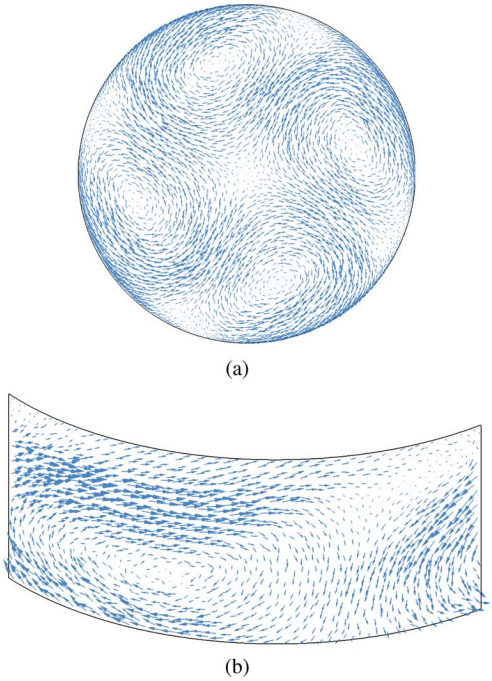

Fig. 8. The distribution of the instantaneous eddy current: (The direction of an arrow denotes the direction of the eddy current, and the length of an arrow denotes the magnitude.) (a) within the surface of the end shield; (b) within the surface of the frame corresponding to one pole pitch. ($r_1 = h_1 = 20$ mm).

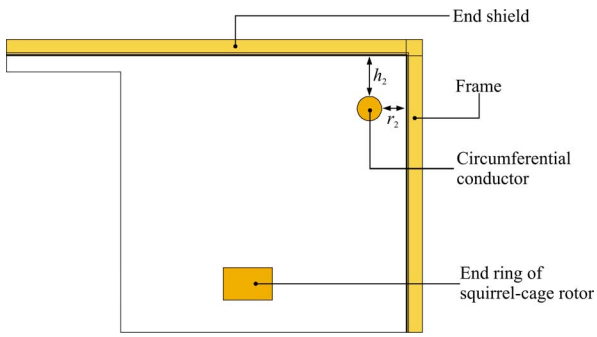

Fig. 9. The simplified 2-D axisymmetric numerical model with two locally defined variables r_2 and h_2 marked.

III. 2-D Analyses of Eddy Current

A. Simplified 2-D Numerical Model

The magnetization curve of the steel of the end shield and frame is nonlinear. Consequently, to study the changes in the eddy-current loss in the nonlinear case, simplified 2-D axisymmetric models were built. Time-stepping FEAs based on a single-valued nonlinear magnetization curve were carried out. For comparison, time-stepping FEAs based on a linear magnetization curve were also completed.

Fig. 9 shows the 2-D axisymmetric model. In the model, the end shield and frame as well as the end ring of the squirrel-cage rotor were included. The 3-D stator end-winding was represented by a 2-D circumferential conductor. The stator and rotor cores as well as the shaft were not included. Instead, suitable boundary conditions were enforced. Furthermore, to model the eddy current accurately, a many-layered mesh was made within a thin layer close to the inner boundaries of the end shield and frame.

B. Time-Stepping FEAs

In the time-stepping FEAs, the governing equation was

$$\nabla\times[\nu(\nabla\times\boldsymbol{A})]+\sigma\frac{\partial\boldsymbol{A}}{\partial t}-\boldsymbol{J}_{\mathrm{s}}=0 \tag{8}$$

where ν is reluctivity; and $\boldsymbol{A}$ and $\boldsymbol{J}_{\mathrm{s}}$ are magnetic vector potential and source current density, respectively.

In the 2-D axisymmetric analyses, $\boldsymbol{A}$ and $\boldsymbol{J}_{\mathrm{s}}$ only have circumferential components, A_{φ} and $J_{\mathrm{s},\varphi}$. Two time-varying sinusoidal currents with the same rms values were applied to the circumferential conductor and end ring, respectively, but the currents were 180° out of phase. Inside the end shield and frame, $\sigma(\partial A_{\varphi}/\partial t)$ was considered.

In both the nonlinear case and linear case, there were 100 time-steps in one time period 0.02 s, and five periods in total were computed for each model.

C. Variation in Eddy-Current Loss

Like the situation in the 3-D FEAs, two locally defined variables, the shortest radial distance r_2 and shortest axial distance h_2, as marked in Fig. 9, were altered from 5 mm to 40 mm by shifting the conductor. The arithmetic mean value of the eddy-current loss per unit circumferential length $\bar{P}^{\varphi}_{\mathrm{Ft}}$, which is adopted in Fig. 10, was computed by

$$\bar{P}^{\varphi}_{\mathrm{Ft}}=\frac{1}{T}\int_0^T\int_{\Gamma_2}\sigma\left(\frac{\partial A_{\varphi}}{\partial t}\right)^2\mathrm{d}S\,\mathrm{d}t \tag{9}$$

where T means a period; Γ_2 means the surfaces of the end shield and frame, as marked in light yellow in Fig. 9.

i) $5\ \mathrm{mm}\le r_2\le 40\ \mathrm{mm}, h_2\equiv 50$ mm: The changes in the eddy-current loss per unit circumferential length within the end shield and frame is plotted in Fig. 10(a). Whether in the nonlinear case or the linear case, a smooth decline in the loss per unit circumferential length within the frame is much more evident than that within the end shield, as r_2 increases. Besides, whether within the end shield or the frame, the loss per unit circumferential length in the nonlinear case is larger than that in the linear case at the same r_2, but the difference between these two cases gets smaller gradually as r_2 becomes larger.

ii) $5\ \mathrm{mm}\le h_2\le 40\ \mathrm{mm}, r_2\equiv 30$ mm: Fig. 10(b) shows the changes in the eddy-current loss per unit circumferential length within the same parts as discussed above. All the curves go down, when h_2 becomes large, but the two curves corresponding to the end shield decline more evidently than the other two curves. The difference between the nonlinear case and linear case gets smaller gradually as h_2 increases.

D. Distribution of Magnetic Induction Lines

Fig. 11 illustrates the distribution of the magnetic induction lines at the instant when the current reaches the peak value. It is clear that due to the skin effect, most of the magnetic induction lines are concentrated inside a thin layer close to the inner boundaries of the end shield and frame. Correspondingly, the eddy current is induced inside the thin layer.

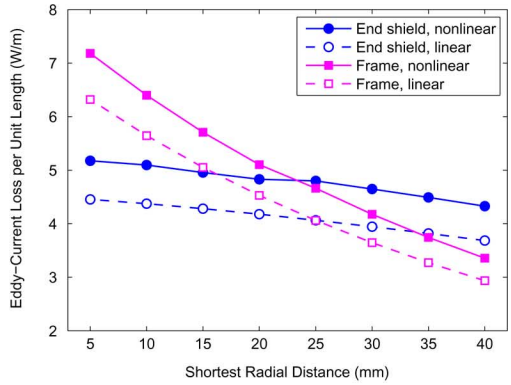

(a)

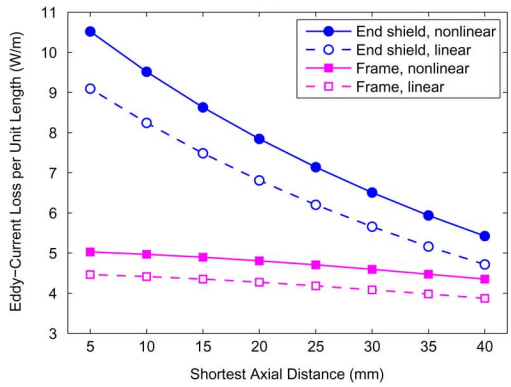

(b)

Fig. 10. The changes in the eddy-current loss per unit circumferential length within the end shield and frame of one end: (a) $5\ \mathrm{mm}\le r_2\le 40\ \mathrm{mm}, h_2\equiv 50$ mm; (b) $5\ \mathrm{mm}\le h_2\le 40\ \mathrm{mm}, r_2\equiv 30$ mm.

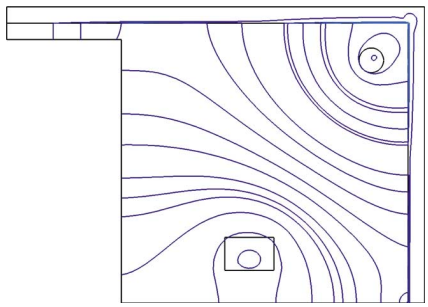

Fig. 11. The distribution of the magnetic induction lines within the end region of one end at the instant when the current reaches the peak value. ($r_2=h_2=30$ mm).

IV. Conclusions and Discussion

In this paper, by proposing a method using the standard impedance boundary condition (SIBC), analyzing the eddy current within the end shield and frame of a large induction machine by FEM becomes possible. The model was validated by the measurement, so the proposed method as well as the parameters of the model proves feasible and accurate in the analysis of the eddy current. The eddy-current loss within the end shield and frame is quite small, for instance, by comparison with the total copper loss within the stator winding. High eddy-current loss mainly distributes within the inner surfaces of these structures that are close to the nose parts of the coil ends. In addition, as the distance between the frame and coil

ends (r_1 in Fig. 5) increases, there is a smooth decrease in the loss. The same situation happens when the distance between the end shield and coil ends (h_1 in Fig. 5) increases. Finally, by using 2-D FEAs, under the same conditions, the loss within the end shield and frame by using a single-valued nonlinear magnetization curve is larger than a linear one equal to 1000.

During the quantitative determination of the loss within the end shield and frame, the proposed measurement method proves to be feasible and easy to operate in the measurement. Two main points should be emphasized. Firstly, the temperature sensors should be placed in such positions that large temperature gradients can be measured, so it, to some extent, needs a basic understanding of the distribution of temperature, which can be obtained from 3-D FEAs. Secondly, the derivatives of temperature with respect to time should be calculated according to the data recorded at the beginning of the measurement, otherwise heat transfer will make the calculated derivatives inaccurate.

In sum, the proposed method makes it possible to deal with the eddy current flowing inside the thin layer close to the surfaces of the conducting structures in the end region. The main limitations lie in that only the fundamental in time is taken into account and other harmonics in time are all omitted. To analyze the effect of the harmonics on the eddy current in the end region, 3-D time-stepping FEAs are needed, but they are quite challenging at present, in particular, for the complex end region of a large rotating electric machine.

ACKNOWLEDGMENT

This work was supported by the Finnish Foundation for Technology Promotion in Finland and the Helsinki University of Technology in Finland. The authors thank the ABB Corporation in Finland for providing the electric machine.

REFERENCES

[1] A. G. Jack and B. C. Mecrow, "A method to calculate turbogenerator end region fields and losses and validation using measured results," *IEEE Trans. Energy Convers.*, vol. EC-2, no. 1, pp. 100–107, Mar. 1987.

[2] M. T. Holmberg, "Three-Dimensional Finite Element Computation of Eddy Currents in Synchronous Machines," Ph.D. dissertation, Chalmers Univ. Technol., Gothenberg, Sweden, Dec. 1998.

[3] B. C. Mecrow, A. G. Jack, and C. S. Cross, "Electromagnetic design of turbogenerator stator end regions," *Proc. IEE*, vol. 136, no. 6, pp. 361–372, Nov. 1989.

[4] V. C. Silva, Y. Maréchal, and A. Foggia, "Surface impedance method applied to the prediction of eddy currents in hydrogenerator stator end regions," *IEEE Trans. Magn.*, vol. 31, no. 3, pp. 2072–2075, May 1995.

[5] K. Yamazaki *et al.*, "Eddy current analysis considering lamination for stator core ends of turbine generators," *IEEE Trans. Magn.*, vol. 44, no. 6, pp. 1502–1505, Jun. 2008.

[6] V. C. Silva, G. Meunier, and A. Foggia, "A 3D finite-element computation of eddy currents and losses in the stator end laminations of large synchronous machines," *IEEE Trans. Magn.*, vol. 32, no. 3, pp. 1569–1572, May 1996.

[7] X. Wen, R. Yao, and J. A. Tegopoulos, "Transient quasi-3D method in the transient electromagnetic field calculation of end region of turbogenerator," *IEEE Trans. Magn.*, vol. 30, no. 5, pp. 3709–3712, Sep. 1994.

[8] E. Schmidt, G. Traxler-Samek, and A. Schwery, "Influence of higher harmonics in the end region magnetic field on eddy currents in the stator clamping system of hydro generators," in *Proc. Int. Electric Machines and Drives Conf.*, San Antonio, TX, May 2005, pp. 1268–1274.

[9] Y. Yao, H. Xia, G. Ni, X. Liang, S. Yang, and P. Ni, "3-D eddy current analysis in the end region of a turbogenerator by using reduced magnetic vector potential," *IEEE Trans. Magn.*, vol. 42, no. 4, pp. 1323–1326, Apr. 2006.

[10] Y. Liang, H. Huang, and G. Hu, "Numerical calculation of end region electromagnetic field of large air-cooled turbogenerator," in *Proc. World Automation Congr.*, Hawaii, Sep./Oct. 2008, pp. 1–5.

[11] Y. Yao, H. Xia, G. Ni, X. Liang, and Z. Xian, "Analysis of magnetic-thermal coupled fields in the end region of large turbine-generators," in *Proc. World Automation Congr.*, Hawaii, Sep./Oct. 2008, pp. 1–5.

[12] Y. Liang, Y. Lu, K. Zhu, B. Ge, and W. Cai, "Analysis and computation of 3D eddy current in turbogenerator rotor end region at asynchronous operation," in *Proc. IEEE Int. Electric Machines and Drives Conf.*, Madison, WI, Jun. 2003, vol. 1, pp. 415–418.

[13] K. Takahashi, K. Hattori, A. Nakahara, and M. Saeki, "Three dimensional harmonic field and eddy current analysis for rotor end region of turbine generator," in *Proc. IEEE Int. Electric Machines and Drives Conf.*, Antalya, Turkey, May 2007, vol. 1, pp. 477–481.

[14] R. Lin and A. Arkkio, "Calculation and analysis of stator end-winding leakage inductance of an induction machine," *IEEE Trans. Magn.*, vol. 45, no. 4, pp. 2009–2014, Apr. 2009.

[15] P. Alotto, A. De Cian, G. Molinari, and M. Rossi, "Implementation of surface impedance boundary conditions in the cell method via the vector fitting technique," *COMPEL: Int. J. Compu. Math. Elect. Electron. Eng.*, vol. 26, no. 3, pp. 859–872, 2007.

[16] J. Gyselinck, P. Dular, C. Geuzaine, and R. V. Sabariego, "Surface-impedance boundary conditions in time-domain finite-element calculations using the magnetic-vector-potential formulation," *IEEE Trans. Magn.*, vol. 45, no. 3, pp. 1280–1283, Mar. 2009.

[17] D. J. Hoppe and Y. Rahmat-Samii, *Impedance Boundary Conditions in Electromagnetics*, 1st ed. Washington, DC: Taylor & Francis, 1995.

Ranran Lin (S'09) was born in Beijing, China, in 1980. He received the B.Sc. degree in engineering from the Shanghai Jiao Tong University, Shanghai, China, in 2002, and the M.Sc. degree in technology from the Helsinki University of Technology, Espoo, Finland, in 2004.

At present, he is a Research Scientist with the Department of Electrical Engineering, Faculty of Electronics, Communications and Automation, School of Science and Technology, Aalto University, Espoo, Finland. His current research interests include the numerical analysis of electromagnetic field and mechanical vibrations in the end region of large rotating electric machines. He was a Session Chair of 2008 IEEE International Magnetics Conference held in Madrid, Spain.

Ari Haavisto was born in Huittinen, Finland, in 1968. He received the B.Sc. degree in electrical engineering from the Satakunta University of Applied Sciences, Pori, Finland, in 1994, and the M.Sc. degree in technology from the Helsinki University of Technology, Espoo, Finland, in 2006.

At present, he is an Operations Engineer with the Department of Electrical Engineering, Faculty of Electronics, Communications and Automation, School of Science and Technology, Aalto University, Espoo, Finland. His current research interests include the thermal modeling of electric machines.

Antero Arkkio was born in Vehkalahti, Finland, in 1955. He received the M.Sc. degree in technology and the D.Sc. degree in technology from the Helsinki University of Technology, Espoo, Finland, in 1980 and 1988, respectively.

He has been working with various research projects which deal with the modeling, design, and measurement of electric machines. At present, he is a Professor of electrical engineering at the School of Science and Technology, Aalto University, Espoo, Finland. He was a Senior Research Scientist and then a Laboratory Manager at Helsinki University of Technology.